# Tailoring experimental configurations to probe transition dipoles of fluorescent nano-emitters by polarimetry or Fourier imaging with enhanced sensitivity

Jiawen Liu, Agnès Maître, Laurent Coolen

## ▶ To cite this version:

HAL Id: hal-03356071

https://hal.sorbonne-universite.fr/hal-03356071v1

Submitted on 27 Sep 2021

# Tailoring experimental configurations to probe transition dipoles of fluorescent nano-emitters by polarimetry or Fourier imaging with enhanced sensitivity

*Jiawen Liu[1], Agnès Maître[1] and Laurent Coolen[1,\*]*

[1]Sorbonne Université, CNRS, Institut de NanoSciences de Paris, INSP, F-75005 Paris, France

ABSTRACT. Probing the transition dipoles responsible for the luminescence of a nano-emitter is essential to understand its physical properties, its interactions with its environment and its potential applications. Various methods in photoluminescence microscopy, based on polarimetry or Fourier imaging, have been developed to measure an emitter's dipole properties : number of radiating dipoles, oscillator strength ratio between them, their orientation etc. In this paper, we model the most used of these protocols and show that their sensitivity depends crucially on the experimental conditions : substrate material, presence of another lower or upper layer, objective numerical aperture. We develop guidelines to optimize the measurement sensitivity by tailoring the experimental conditions, depending on the type of protocol used and the dipole property to be measured.

# 1. INTRODUCTION

Since the first solid-state detections of single-molecule luminescence[1,2], numerous efforts have been made to measure the properties of the optical transition dipole moment responsible for the luminescence. In particular, in order to understand the underlying physics of a nano-emitter (molecule, colored center, semi-conductor nanoparticle, two-dimensional – 2D – semiconductor system etc.), its dipolar orientation is of paramount interest. A correlated crucial question is whether the emitter behaves as a single linear radiating dipole, or whether it must be described as an incoherent sum of two or three dipoles, because several degenerated transitions contribute to the emission. For instance, a "2D dipole" model (sum of two orthogonal dipoles of same oscillator strength) has been used to describe spherical colloidal quantum dots[3-5], dot-in-plates[6] or square nanoplatelets[7-9] and could also apply to some molecules or colored centers[10]. Rectangular nanoplatelets were shown to behave as a sum of two orthogonal dipoles of different oscillator strengths[9] while three orthogonal dipoles were necessary to model a chain of self-assembled nanoplatelets[11]. For 2D sheets of semiconductors, in-plane dipoles were evidenced with $MoS_2$ [12], $MoSe_2$ and $WSe_2$ [13] while layered InSe flakes displayed a single out-of-plane dipole[13]. For luminescent Eu-doped films, the contribution of both electric and magnetic transition dipoles has been demonstrated[14].

Beyond its fundamental importance, the measurement of the number and orientations of the radiating dipoles is essential to understand light-matter interactions at the single-emitter scale as well as non-radiative near-field coupling mechanisms[15]. For example, in plasmonic structures, since local electric fields orient vertically to the metal substrate, a stronger plasmonic coupling between emitters and metals can be achieved when the emitters present vertical dipoles. Förster

resonant energy transfer (FRET) is also more efficient between emitters of parallel dipole moments[8,16]. Furthermore, dipole anisotropy and orientation can be used to tailor the efficiency of opto-electronic devices such as light-emitting diodes[17]. The orientation of a single luminescent dye can also be used to track distortions in amorphous media[18] or movements of single proteins in living cells[19,20].

Various strategies have been proposed to probe the number and orientation of radiating dipoles in nano-emitters. A first range of methods used polarimetric analysis of the luminescence, either by decomposition into several polarization components[20,21] or by using a rotating polarizer to measure the degree of polarization[3,4,22]. A second class of methods uses the radiation pattern (angular distribution of the emission) measured by Fourier (back focal plane) imaging[9,11,23,24] or indirectly by defocused imaging[19,25-27]. A widespread variant used polarized Fourier imaging to distinguish in-plane and out-of-plane dipole contributions[7,8,12-14,28]. Various other protocols have been introduced, such as separating different emission directions with an annular plate[29], comparing degrees of polarization with different collection apertures[30], using imaging aberrations[26,31], probing the effect of a nearby interface on decay dynamics[5, 32], separating spectrally the electric and magnetic contributions[33] etc.

All of these methods rely on comparing the *measured observable* (degree of polarization, Fourier image etc) with the result of a model involving the dipole(s) and its(their) orientation, which is the *unknown quantity* of interest. It is well known that this model must take into account radiation modifications introduced by the proximity of an optical interface (substrate surface, protective layer, underlying dielectric spacer etc), as it may partially reflect the radiation[15,22,23]. The objective numerical aperture is also a key parameter. Some of us have mentioned in several papers[9,11,22,24] that the choice of these *experimental conditions* (interface within the optical

environment, objective numerical aperture) can either favor or prevent the determination of the unknown quantities. However, this point was never examined in detail.

In this paper, we model the effect of the experimental conditions on three typical protocols : polarization analysis, polarized Fourier imaging and unpolarized Fourier imaging, used to determine either the emitter's number of contributing dipoles or dipole orientation. We define figures of merit to assess the sensitivity of each protocol and use them to compare several common experimental conditions as examples. We show that the experimental conditions can, in some cases, create redhibitory difficulties to extract the unknown quantities, but can also be tailored to provide optimized sensitivity. This optimization will depend on the quantity to be measured, so that it is critical to design the configuration carefully. The purpose of this paper is thus to give a guidance on how to choose the best experimental configuration according to the question to study.

The paper is organized as follows : in the first section, we outline the general experimental methods and theoretical backgrounds. In the next three sections, we successively describe the three protocols of polarization analysis, polarized Fourier imaging and unpolarized Fourier imaging. In each section, we define a relevant figure of merit to quantify the protocol's sensitivity, and then describe which experimental conditions optimize this figure of merit.

## 2. GENERAL PROBLEM

Figure 1 (a) illustrates a typical inverted fluorescence microscope. The emitters are deposited on a substrate, sometimes covered by a protective polymer layer, and excited by a focused laser beam. The fluorescence emission (always calculated for this paper at wavelength 600 nm) is collected by the same objective and sent to various detection devices, such as a photodiode preceded by a rotating polarizer for polarization analysis, or a camera conjugated to the emitter's Fourier plane for radiation pattern measurement.

Depending on how the nano-emitters are modelled, different numbers of unknown quantities will characterize their dipolar emission and be investigated experimentally. Three typical cases are presented on figs. 1(c,d,e). If the emitter is known to behave as a single linear radiating dipole (fig. 1(c)), the only quantity to be probed is its orientation $(\Theta, \Phi)$. It can be obtained from the polarization analysis curve (fig. 1(b)) : the polarizer orientation for which the detection is maximal yields the in-plane (azimuthal) orientation $\Phi$. The degree of polarization $\delta = \frac{I_{max} - I_{min}}{I_{max} + I_{min}}$ can be related to the out-of-plane (zenithal) orientation $\Theta$. Deducing $\Theta$ from the measured $\delta$ requires the theoretical knowledge of the relation $\delta(\Theta)$. This calculation, which will be found in ref. 22, may involve the effect of light transmission or reflection by the optical interface between the substrate and air. It also requires to sum the radiation over all collected angles, so that the result depends on the objective numerical aperture. Throughout the paper, we will call "experimental conditions" the type of substrate used (composition, thickness, presence of a cover layer etc) and the objective numerical aperture. Details about the range of experimental conditions considered are given in Supporting Information (S.I.) section B.

A well-known case of emitter differing from the single linear dipole is the "two-dimensional (2D) dipole" (sum of two orthogonal incoherent dipoles of equal oscillator

strengths), which has been demonstrated for instance for semiconductor nanoparticles[3-9]. In this case, the "2D" dipole is characterized by its orientation $(\Theta, \Phi)$, defined as the orientation of the axis normal to the 2 dipoles (fig. 1(d)). The theoretical relation between $\delta$ and $\Theta$ can also be calculated[22] (S.I. section A) so that the orientation of the 2D dipole can also be obtained by polarimetry.

For some other cases, such as 2D planar materials[12,13] or particle geometries inducing a preferred deposition orientation (nanoplatelets[24], dot-in-plates[6]), the orientation of the emitter is known, but one wishes to investigate the number of incoherent dipoles contributing to the emission or their ratio (fig. 1(e)). In this paper, we will define as $x, y$ and $z$ the eigenaxes of the emitter ($z$ being the optical axis, normal to the sample plane) and $\eta_x$, $\eta_y$ and $\eta_z$ the corresponding oscillator strengths, normalized so that $\eta_x + \eta_y + \eta_z = 1$. If only two of these three dipoles are involved in the luminescence, their ratio is the only unknown quantity and it can be deduced from the degree of polarization[9], as will be shown below. If the three orthogonal dipoles are to be probed, then the measured degree of polarization alone cannot provide enough information to answer the question.
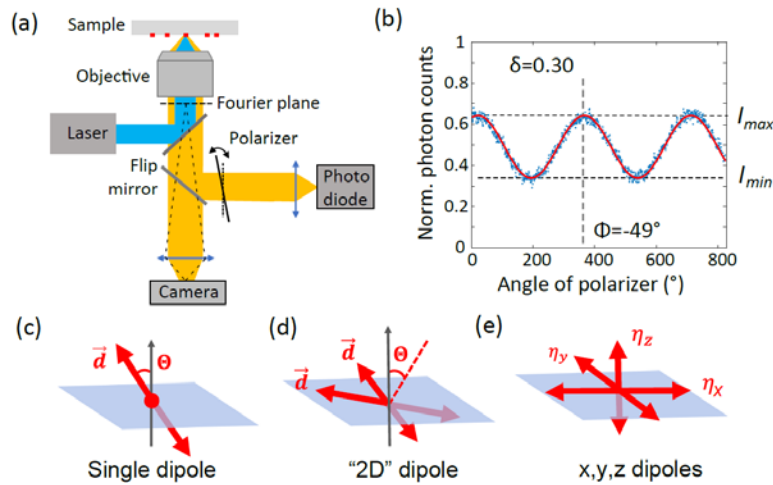
**Figure 1.** (a) Schematic of a typical microphotoluminescence setup. (b) Typical experimental polarimetry curve : the measured intensity is plotted as a function of the polarizer orientation and fitted by a cosine function, from which the degree of polarization (here δ=0.30) is extracted. (c, d, e) Three main questions about a radiating nano-emitter : its orientation $(\Theta, \Phi)$ if it is a single linear dipole (c) or a "2D" dipole (d), its contributions $\eta_x$, $\eta_y$ and $\eta_z$ if it has two in-plane and one out-of-plane dipole (e).

More information is then obtained by Fourier plane imaging (fig. 1(a)). In microscopy, the Fourier plane is the back focal plane of the objective, which can be conjugated by a lens onto a CCD camera (details in ref. 24). The emission intensity distribution in the Fourier plane (fig. 4(a)) is a measure of the radiation pattern (emission angular distribution in the far field) defined as $I(\vec{k}) = dP/d\Omega$ (where $dP$ is the power radiated within a solid angle $d\Omega$ centered on $\vec{k}$), as each point in the Fourier plane corresponds to a specific emission angle (the radiation pattern is obtained experimentally by dividing the Fourier image by the apodization factor $\cos\theta$, where $\theta$ is the angle between $\vec{k}$ and the $z$ axis, describing the ratio between an area $dS$ in the Fourier plane and a solid angle $d\Omega$ in the radiation space). For example, in a recent paper, we used Fourier imaging combined with polarimetry to probe quantitatively the 3 dipole components $\eta_x$, $\eta_y$ and $\eta_z$ in stacked chains of nanoplatelets[11]. The dipole components are then obtained by fitting the Fourier image with the theoretical radiation patterns, which again take into account the experimental conditions (substrate, objective etc)[15].

Combining Fourier imaging and polarization analysis would be quite challenging for a single nano-emitter, but it has been performed for various ensembles of dipoles, for instance on a layer of nanoplatelets to analyze the ratio between in-plane and out-of-plane dipoles (which

determines its efficiency as a light-emitting device) [17], or on rare-earth ions to compare the contributions of electric and magnetic dipoles[14,33].

Other microscopy methods exist for analysing a radiating dipole. For instance, a slightly defocused image can be used to distinguish single linear dipoles from 2D dipoles and measure their orientation[19, 25-27]. This method is experimentally simple, but involves slightly more complex theoretical calculations and increased influence of aberrations[23], so that we will not discuss it here, although the same general conclusions about the importance of the experimental conditions should also apply for defocused imaging.

To summarize this section, we have defined several *measured observables* (degree of polarization, Fourier image) and several *unknown quantities* which can be of interest ($\Theta$, $\eta_y$, $\eta_z$ etc.). A measurement protocol will thus consist in deducing the unknown quantity from its theoretical relation with the measured observable. In order for a protocol to be efficient, *the measured observable must have a strong dependence on the unknown quantity*. We will in the next sections, for several typical protocols, define a *figure of merit quantifying this dependence*, and identify under which experimental conditions this figure of merit is optimal.


## 3. POLARIZATION ANALYSIS

The measured polarization is a result of the field radiated into all directions within the objective numerical aperture. Figure 2(a) shows the two extreme cases in which the zenith angle is 0° ("out-of-plane (OP) dipole" or "*z* dipole") and 90° ("in-plane (IP) dipole" or "*x* or *y* dipole") respectively. As appears in the projection plane, the overall emission is not polarized for the OP dipole whereas it is maximally polarized for the IP dipole. Intermediate degrees of polarization

are obtained either when the dipole orientation is between 0 and 90° or when the emitter behaves as a sum of two or three dipoles.

When the emitter is known to behave as a single linear dipole or as a "2D dipole", the degree of polarization can be expressed as a function of the dipole orientation :

$$\delta(\Theta)_{1D} = \frac{C \cdot sin^2\Theta}{(2A-2B+C) \cdot sin^2\Theta + 2B} \qquad \delta(\Theta)_{2D} = \frac{C \cdot sin^2\Theta}{-(2A-2B+C) \cdot sin^2\Theta + 4A + 2C} \qquad (1)$$

where $A$, $B$ and $C$ are coefficients defined in ref. 22 as a function of the optical environment (substrate index etc) and of the objective numerical aperture. In most cases $A$ is much smaller than $C$ (fig. S2(a) and (b)), so that, at least for a qualitative analysis of the problem, we can take $2A/C \sim 0$ (if this approximation is not valid, the general degree of polarization decreases but the qualitative observations below remain true : see fig. S2(c)). The effect of the experimental conditions on the function $\delta(\Theta)$ is then solely described by the factor $f_1 = \frac{2B}{C}$ :

$$\delta_{1D}(\Theta) = \frac{sin^2\Theta}{(1-f_1)sin^2\Theta + f_1} \quad ; \quad \delta_{2D}(\Theta) = \frac{sin^2\Theta}{(f_1-1)sin^2\Theta + 2} \qquad (2)$$

Figure 2 plots the function $\delta(\Theta)$ in the case of a single dipole (b) and a 2D-dipole (c) as given by equation (2) for different values of $f_1$. The orientation $\Theta$ can be deduced with the best resolution from the measured $\delta$ if the slope of this curve is strong. For a single dipole, a configuration with $f_1 \sim 1$ provides a good resolution for a large range of $\Theta$, so that $f_1 \sim 1$ is the condition that should be most generally looked for. However, if smaller $\Theta$ values can be anticipated (dipole almost OP), it is best to have a strong $\delta(\Theta)$ slope at low $\Theta$, which is obtained for $f_1 \ll 1$. On the other hand, the protocol can be made more sensitive for larger $\Theta$ (nearly IP dipoles) by choosing $f_1 \gg 1$.

In other words, in the polarimetry measurement, coefficients $B$ and $C$ (still considering that $A$ is negligible) describe respectively to which extent the detected intensity will

depend on $\cos \Theta$ (OP dipole component) and on $\sin \Theta$ (IP dipole component) (see S.I. - A). Therefore, for a large value of $f_1 = 2B/C$, the effect of the OP dipole on polarization will be stronger, so that a weak OP component (large $\Theta$) will be better detected, and vice versa for a small $f_1$.

A different result is found for a "2D" dipole (fig. 2(c)) : large values of $f_1$ lead to a very low degree of polarization, so that $f_1$ should be as small as possible for a better resolution (whatever the expected range of $\Theta$ values).
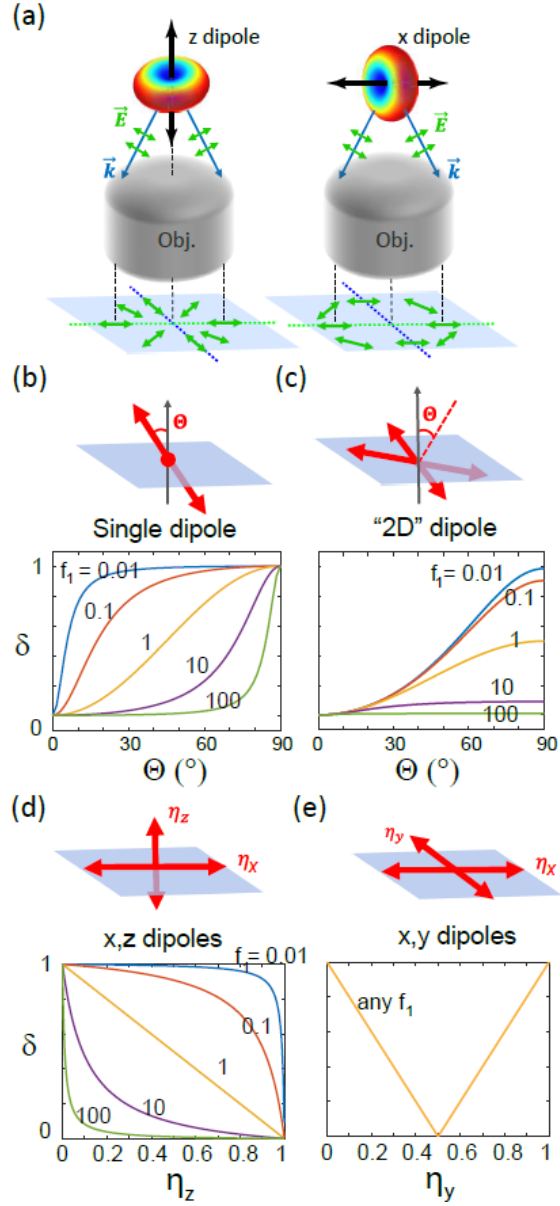
**Figure 2.** (a) Schematic of the radiated polarization for an out-of-plane or an in-plane dipole. (b,c) Degree of polarization δ as a function of the orientation Θ, for various values of $f_1$, for (b) a single linear dipole and (c) a "2D" dipole. (d, e) Degree of polarization δ, for various values of $f_1$, as a function of (d) the $\eta_z$ dipole contribution (if $\eta_y = 0$) or (e) the $\eta_y$ dipole contribution (if $\eta_z = 0$).

We now turn to the case of three dipoles of known orientations $x, y$ or $z$ with unknown oscillator strengths normalized by $\eta_x + \eta_y + \eta_z = 1$. If only the degree of polarization is known, the problem cannot be solved in the general case of three dipoles, but it can be if the presence of only two dipoles can be assumed :

- for one IP dipole $\eta_x$ and one OP dipole $\eta_z$ (thus $\eta_y = 0$), as demonstrated experimentally for a cubic nanoplatelet standing on its edge for instance [24], we find (see S.I. - A):

$$\delta = \frac{1-\eta_z}{1+(f_1-1)\cdot\eta_z} \tag{3}$$

A value $f_1 \sim 1$ provides a clear dependence of $\delta$ on $\eta_z$ for all $\eta_z$ values (fig. 2(d)), so that this case is in general the best for this measurement. However a large $f_1$ might be better to precisely study a very weak OP dipole, while a small $f_1$ would be more appropriate to probe a weak IP dipole. Again, the reason is that coefficients $B$ and $C$ respectively describe whether OP and IP dipoles will have a strong effect on the measured polarization.

- for only two IP dipoles ($\eta_z = 0$), as evidenced for instance on rectangular nanoplatelets deposited horizontally[9], we have $\delta = |\eta_x - \eta_y|$ for any experimental condition. The degree of polarization is then solely dependent on the emitter, regardless of the experimental configurations : any value of $f_1$ will work (fig. 2(e)). The factor $f_1$ has no importance here because only IP dipoles are probed.

Eventually, the optimal choice of $f_1$ for each unknown information to be extracted precisely from the degree of polarization is summarized in Table 1.

12

| Unknown quantity to be measured | Optimal $f_1$ |
|---|---|
| Orientation of a single dipole (broad range of Θ) (fig. 2(b)) | ≈ 1 |
| Orientation of a single dipole (close to OP) (fig. 2(b)) | ≪ 1 |
| Orientation of a single dipole (close to IP) (fig. 2(b)) | ≫ 1 |
| Orientation of a "2D dipole" (fig. 2(c)) | ≪ 1 |
| Ratio between two dipoles, one IP, one OP (fig. 2(d)) | ≈ 1 |
| Ratio between two IP and OP dipoles, if OP is weak (fig. 2(d)) | ≫ 1 |
| Ratio between two IP and OP dipoles, if IP is weak (fig. 2(d)) | ≪ 1 |
| Ratio between two orthogonal IP dipoles (fig. 2(e)) | any value |

**Table 1 :** optimal condition on factor $f_1$ for each polarization measurement

Different experimental configurations will lead to very different values of $f_1$. For example, in Figure 3(a), we consider an emitter within a medium of index 1.5, observed with an oil objective (N.A.=1.4), at a distance $z_0$ from an interface with a second, upper medium (more configurations are analysed in fig. S3). This upper medium can for instance be air (emitter on a glass substrate and covered by a $z_0$ protective polymer layer of index 1.5) or another material such as gold or silver (corresponding to a metallic substrate covered by a $z_0$ silica spacer) (see S.I. section B). We plot the $f_1$ values for $z_0 = 100$ nm as a function of the real and imaginary indices ($n$ and $k$) of the upper medium. Small values of $f_1$ are then obtained for a metallic substrate, especially silver, while $f_1$ is larger than unity when the upper medium is air, and can be tuned to unity or lower values by using a dielectric upper medium of higher index.
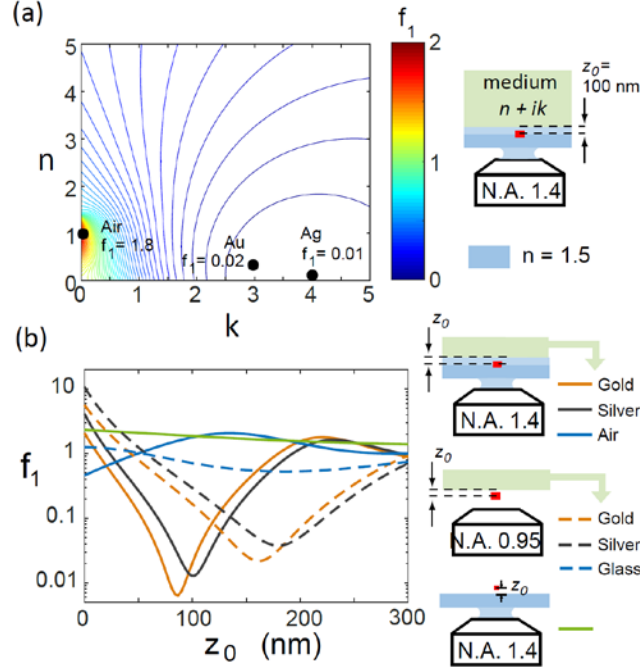
**Figure 3.** Value of the factor $f_1$ for an emitter at a distance $z_0$ from an optical interface. (a) Emitter in a medium of index 1.5, second medium of complex index $n + ik$, contour plot of the dependence $f_1(n, k)$ for $z_0 = 100$ nm. (b) Emitter in several typical conditions, dependence $f_1(z_0)$.

Eventually, we compare seven common experimental cases in figure 3(b) and calculate their theoretical values of $f_1$ as a function of the parameter $z_0$. If $f_1 \sim 1$ is desired, a glass substrate and an oil objective may be chosen, and a polymer cover layer of thickness $z_0 = 50$ nm can be added in order to achieve precisely $f_1 = 1$. A glass substrate with an air objective also leads to $f_1 \sim 1$. However, among these cases, using the oil objective with a glass substrate leads to non-negligible values of $2A/C$ (fig. S2(b)), thus to an overall decrease of the degree of polarization (fig. S2(c)), so that the air objective case may be preferred (however at the cost of lower detected luminescence intensity).

14

Alternatively, metallic substrates offer a much broader choice of $f_1$ values, which can be of interest in certain cases as listed in Table 1. Interferences between direct and reflected radiations are responsible for these strong variations, as evidenced by the dependence on $z_0$. If $f_1 \gg 1$ is needed, a spacer thickness $z_0 \sim 0$ should be used (provided that not too many losses are induced by the proximity to the metal) and up to $f_1 \sim 10$ can be obtained with a silver substrate. If $f_1 \ll 1$ is requested, the spacer thickness should be adjusted between 80 and 200 nm depending on the metal and $f_1$ can be decreased as low as 0.006.

## 4. POLARIZED FOURIER IMAGING

We now turn to Fourier plane imaging protocols, starting with the polarization-resolved analysis (fig. 4(a)) of an ensemble of emitters with random isotropic in-plane orientation (sum of three dipoles with $\eta_x = \eta_y$), as performed in refs. 7,8. Figure 4(b) simulates the Fourier plane images of $x, y$ and $z$ dipoles (corrected by the apodization factor $\cos \theta$, where $\theta$ is the angle between $\vec{k}$ and the $z$ axis) filtered by a polarizer oriented along the $x$ axis. The $y$-dipole contribution is completely filtered by the polarizer along the $k_x$ axis, so that the measured image profile along the $k_x$ axis will be a sum of the $x$ (IP) and $z$ (OP) dipoles contributions. The experimental protocol will thus consist in plotting the radiation pattern profile $I(k_x, k_y = 0)$ as a function of $k_x$ and fit the theoretical model by adjusting the ratio between the IP and OP dipole components[7].
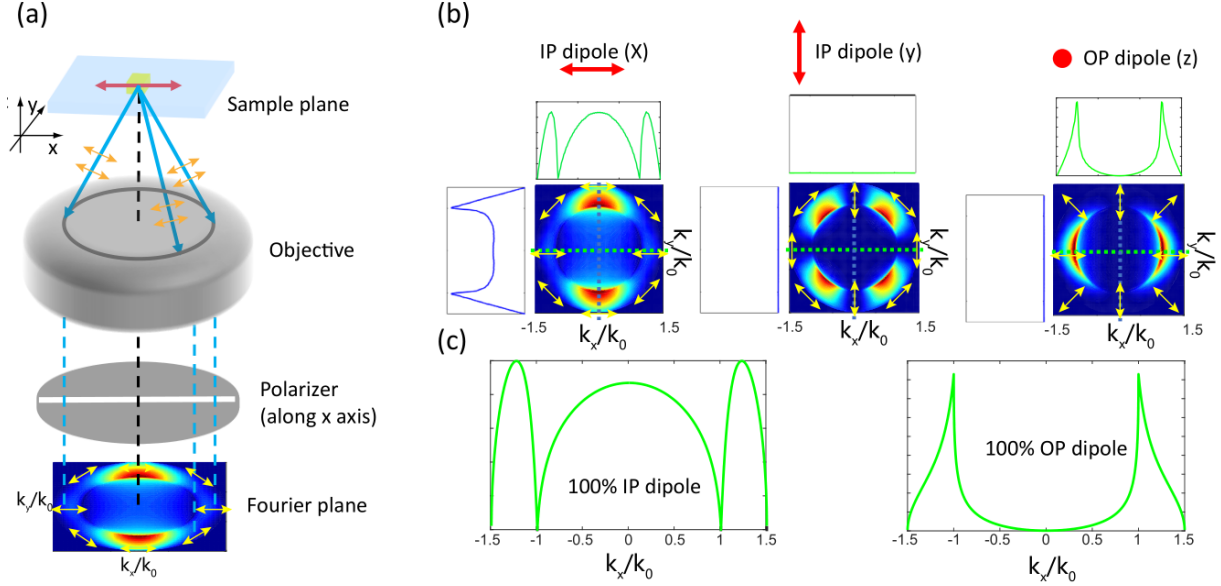
**Figure 4.** (a) Polarized Fourier imaging schematic (electric-field shown as yellow arrows). (b) Polarized Fourier images of *x*, *y* and *z* dipoles respectively, with cross-section profiles of the Fourier plane image cut along the $k_x$ axis (green curves) and $k_y$ axis (blue curves – profiles obtained analytically and Fourier image from FDTD simulations, both corrected by the apodization factor $\cos\theta$). (c) Cross-section profile of the radiation pattern (angular distribution of emission) of a 100% in-plane dipole (left) and a 100% out-of-plane dipole (right) on top of a glass slide observed by an oil objective.

Figure 4 (c) shows the $x$-axis profile of the radiation pattern $I(k_x)$ (with $k_y = 0$). In order to measure an accurate IP/OP ratio by fitting the experimental radiation pattern, we need the IP and OP radiation pattern profiles to be very distinct. To quantify how much the radiation profile will change as a function of the ratio between IP and OP dipoles, we introduce a figure of merit $f_2$ as:

$$f_2 = \frac{\int_0^{N.A.} |\partial I(k)/\partial \eta_z|\, dk}{\int_0^{N.A.} I(k)\, dk} \tag{4}$$

16

The numerator includes the partial derivative of $I(k)$ as a function of $\eta_z$ (while keeping $\eta_x +$ $\eta_y + \eta_z = 1$ and $\eta_x = \eta_y$ ), integrated over the whole objective numerical aperture. The denominator is introduced for normalization. We will use this factor $f_2$ (which depends on $\eta_z$) as a figure of merit of the sensitivity of the polarized Fourier imaging in a given experimental condition. Typical high-N.A. objectives lead to a maximal collection angle of about $\theta_{max} = 70°$. However, collection at high angles can induce significant losses[34] and aberrations leading to discrepancies with theory[11]. Thus we chose to calculate $f_2$ by integrating only up to $\theta_{max} = 55°$, meaning that the fit of the experimental curve will be performed most relevantly in that range and not take into account higher angles.

As a first example, Figure 5(a) considers a configuration using a gold substrate, a silica spacer and an oil objective and investigates the effect of the spacer thickness $z_0$ on $f_2$ . We identify $z_0 = 190$ nm as the configuration providing the highest $f_2$ for all values of $\eta_z$ (black dashed line) while the worst configuration corresponds to $z_0 = 80\ nm$ (red dashed line). Indeed, the Fourier profile for $z_0 = 80$ nm is almost the same for all values of $\eta_z$, so the protocol would fail completely under such experimental conditions (fig. 5(b)). On the other hand, the optimized case $z_0 = 190$ nm leads to dramatic changes of the radiation pattern as a function of the IP/OP ratio (fig. 5(c)). This validates $f_2$ as a good figure of merit to identify optimal experimental conditions.
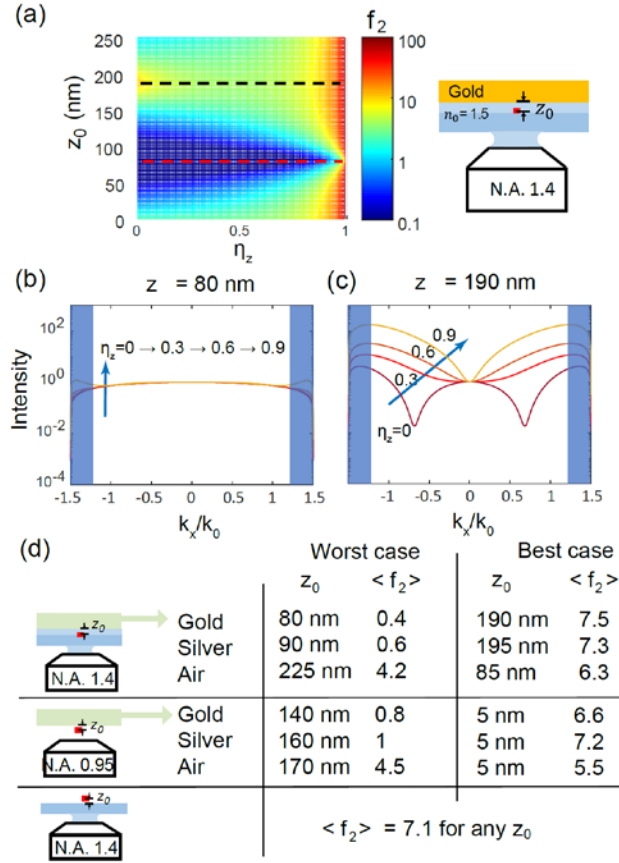
**Figure 5.** With a gold substrate and an oil objective, (a) figure of merit $f_2$ as a function of $\eta_z$ and $z_0$, showing the best (black dotted line) and worst (red dotted line) values of $z_0$ ; (b) and (c) radiation patterns $I(k_x)$ (for $k_y = 0$) for different values of the out-of-plane contribution $\eta_z$, in the (b) worst and (c) best cases (resp. $z_0 = 80$ and 190 nm). The blue shade indicates the high-angle portion that we exclude in our calculation because of potential losses and aberrations. (d) For different configurations, worst and best values of $z_0$ and corresponding figure of merit $f_2$ (averaged over all values of $\eta_z$ between 0 and 1). The last configuration shows no dependence on $z_0$ so that all values are equally good.

We performed the same analysis for various configurations and, for each, worst and best values of $z_0$ were identified. They are summarized, along with the corresponding factor $f_2$

(averaged over all values of $\eta_z$), in fig. 5(d). For configurations using a glass substrate, the differences between the best and worst cases are not very strong (as confirmed when plotting the full radiation patterns : see fig. S4), with no effect of $z_0$ at all for the last configuration. This latter configuration (glass substrate and oil objective with no protective layer, as used in ref. 7) is in fact simple to implement and provides among the best factors $f_2$. When gold or silver substrates are used, the value of $z_0$ is more critical and the worst cases must absolutely be avoided, whereas the best cases offer very good sensitivity.

Finally, we note that polarized Fourier imaging has also been used to quantify the ratio between electric and magnetic dipole contributions from an ensemble of Europium dopants[14]. A similar treatment can be applied to this case and some experimental conditions are shown to be completely inefficient while others are optimal : a full treatment will be found in S.I. section H.


## 5. NON-POLARIZED FOURIER IMAGING


In this last section, we consider the use of Fourier imaging (without polarization selection) to investigate the three dipole coefficients $\eta_x$, $\eta_y$ and $\eta_z$ of a single nano-emitter, as performed in refs. 9, 11, 24. Because here two unknown quantities can be measured (ratios $\eta_y/\eta_x$ and $\eta_z/\eta_x$), this method provides more information than the two previous ones but it is also more complex. It consists in fitting with theory the experimental radiation pattern profiles taken along the two symmetry axes of the Fourier plane : resp. $I(k_x)$ (with $k_y = 0$ ; green lines on fig. 6) and $I(k_y)$ (with $k_x = 0$ ; blue lines on fig. 6).
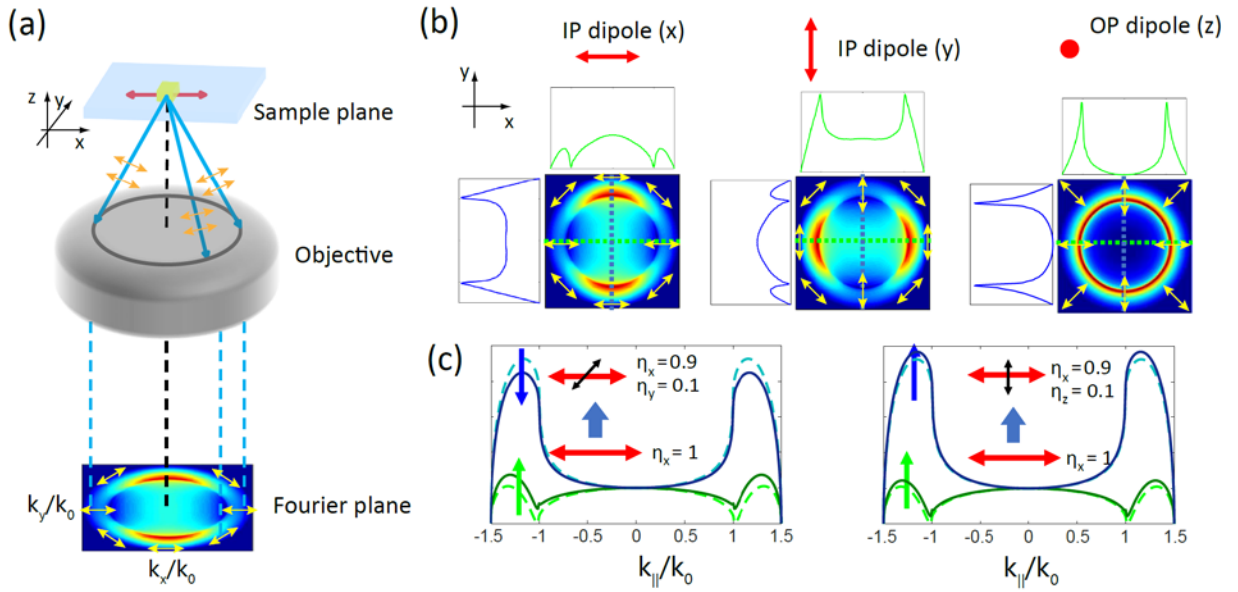
**Figure 6 :** (a) Fourier imaging schematic (without polarization selection ; electric-field shown as yellow arrows). (b) FDTD simulation of Fourier imaging of $x$, $y$ and $z$ dipoles respectively. The panels show cross-section profiles cut along the $x$ axis (green curves) and $y$ axis (blue curves). (c) Cross-section profiles of the Fourier plane for a single horizontal linear dipole (dotted lines) and a linear dipole to which is added a minor IP (left) or OP (right) orthogonal component (full lines). The emitter is observed on a glass slide, covered by a 30-nm of polymer, with an oil objective.

In Figure 6(c), we show the example of a single in-plane dipole ($\eta_x = 1$ ; dotted line). If we add a small portion of $y$-dipole ($\eta_x = 0.9, \eta_y = 0.1$ ; left plot, full line), the $x$-axis profile becomes more intense (its high-angle lobes increase with respect to the emission at normal angle) while the $y$-axis profile decreases. On the other hand, if we add a weak $z$-dipole instead ($\eta_x = 0.9, \eta_z = 0.1$ ; right plot, full line), both $x$- and $y$-axis profiles increase (their lobes increase with respect to emission at normal angle). In the S.I. (fig. S5), we evaluate more cases and draw the

following conclusion: (i) when the OP-dipole contribution ($\eta_z$) is increased, the emission lobes are increased along both profiles $I(k_x)$ and $(k_y)$ ; (ii) when the ratio between the two IP dipoles (ratio $\eta_x/\eta_y$) is changed, the ratio between the lobes of $I(k_x)$ and $I(k_y)$ is changed. Therefore, the typical fitting approach will be to (i) adjust $\eta_z$ so that the height of the lobes matches theory, and (ii) adjust $\eta_y$ so that the ratio between the lobes matches theory.

Note that, in Figure 6(c), all the curves are normalized by the value at normal angle $I(k_x = k_y = 0)$. Therefore the integral area below each curve (here labelled $A_x$ and $A_y$) will reflect the ratio of its high angle lobes with respect to the emission at normal incidence. It can be shown (see S.I.-F) that, in agreement with our qualitative observations above, (i) the sum $S = A_x + A_y$ will be related only to the OP component $\eta_z$, (ii) and the difference $D = |A_x - A_y|$ will be proportional to the difference $|\eta_x - \eta_y|$ between the two IP dipoles, with no direct dependence on the OP dipole. A given measurement configuration will be optimal for our protocol if $S$ depends strongly on $\eta_z$ and if $D$ depends strongly on $|\eta_x - \eta_y|$.

In order to identify optimal configurations, we therefore define two normalized figures of merit, respectively quantifying (i) the dependence of $S$ on $\eta_z$ and (ii) the dependence of D on $\eta_y$ :

$$f_3 = \frac{|\partial S/\partial \eta_z|}{S} \quad , \quad f'_3 = \frac{|\partial D/\partial \eta_y|}{S} \tag{6}$$

Figure 7 compares the potential of Fourier imaging for different experimental configurations (more detailed data can be found in figs. S6 and S7). Figure 7(a) displays values of $f_3$ (for $\eta_z = 0.5$) and $f'_3$. Because the two figures of merit must be optimized at the same time (unless one focuses more on estimating either $\eta_z$ or $\eta_y$), a trade-off must be sought. We then plot the changes induced to the Fourier profiles $I(k_x)$ and $I(k_y)$, either when adding a second $\eta_y$ component to a single $x$ dipole (red and blue curves) or when adding a third $\eta_z$ component to a

21

horizontal "2D" dipole (purple curve). From the $f_3$ and $f'_3$ factors, we can identify potential favorable (fig. 7(d)) and unfavorable (7(c)) values of $z_0$ for glass, gold or silver substrates. Indeed, for the favorable cases, the Fourier profiles show a very clear dependence on both the OP component and the second IP component. Under these experimental configurations, Fourier imaging can thus be used to find accurate values of the three dipole components. Moreover, the gold and silver cases show a significant improvement as compared to the glass substrate (which is why we used a gold substrate in ref. 11). For the unfavorable experimental configurations (fig. 7(c)), on the other hand, the Fourier profiles show negligible changes when adding a second IP dipole, and only weak changes when adding a third OP component. For an emitter on a glass substrate observed by an oil objective, all distances $z_0$ yield the same $f_3$ and $f'_3$ . This configuration is useable (fig. 7(b)), but less efficient than the favorable gold or silver configurations (lower $f'_3$ factor).

Eventually, our results indicate that examples of good configurations, in order to optimize both the $\eta_y$ and $\eta_z$ measurements, are to use an oil objective with gold or silver substrates with a silica spacer of around 200 nm. A glass substrate where the emitters are covered by a 100-nm polymer layer and observed with an oil objective may also be used.
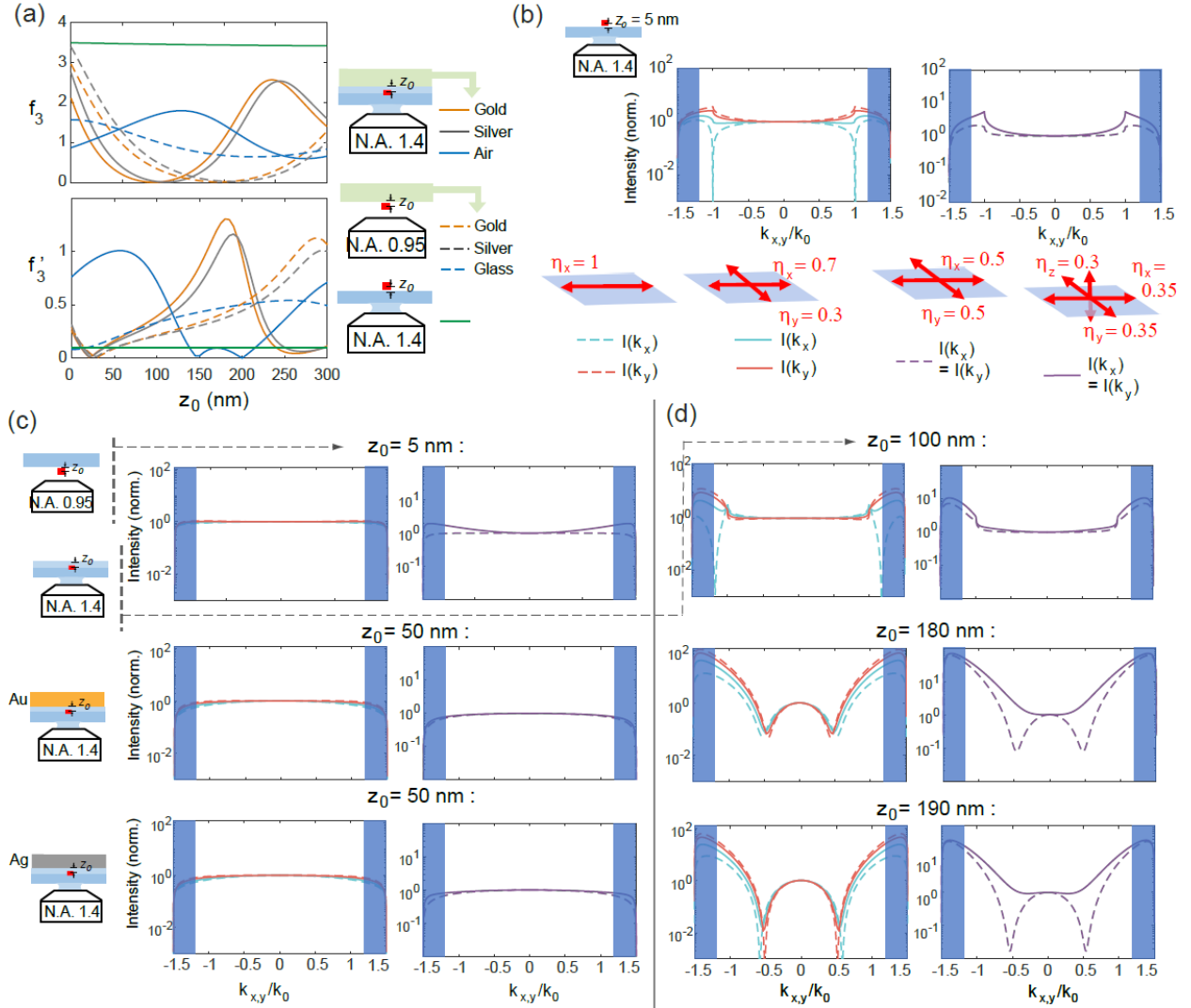
**Figure 7.** (a) Figures of merit $f_3$ (for $\eta_z = 0.5$) and $f'_3$ (valid for any $\eta$'s) as a function of the thickness $z_0$ for 7 different experimental configurations. (b) For an emitter on a glass slide at distance $z_0 = 5$ nm, (c) for various worst configurations, and (d) for various best configurations : radiation patterns $I(k_x)$ and $I(k_y)$ for changing values of $\eta_y$ (left) and $\eta_z$ (right).

## 6. CONCLUSION

In this paper, we gave a theoretical description of three different protocols to analyse the transition dipoles in nano emitters: polarization analysis, polarized Fourier imaging and non-polarized Fourier imaging. We demonstrated that the sensitivity with which these techniques yield transition dipole properties is significantly dependent on the experimental configuration,

23

some conditions being completely redhibitory. We introduced figures of merit to estimate this sensitivity and compared theoretically the performance of different experimental configurations for these protocols, as summarized in Table 1 and Figs 5(d) and 7(d). These guidelines should help to avoid detrimental experimental configurations and choose the best ones to enhance measurement sensitivity.

A remaining question is whether a more general protocol can be established to obtain both the dipoles orientation and oscillator strengths of a single emitter, without any a priori knowledge of either its number of contributing dipoles or their orientation. The approach detailed here could be used to design and optimize such a protocol. Based on our results, a possibility could be to start with polarized Fourier imaging for a first estimate of the IP/OP dipoles ratio, and then switch to non-polarized Fourier imaging for a full measurement of the three dipoles. Using an oil objective and a gold substrate covered by a 180-nm silica spacer would then be a good configuration for both polarized and non-polarized Fourier imaging. The main challenge would then be to demonstrate experimentally whether such a protocol can achieve a reasonable accuracy, given the limited photon count of single-emitter experiments.

This principle of measurement under tailored experimental conditions can be extended to any other protocol used to characterize transition dipoles, for instance defocused imaging. We have restricted our study to nano-emitters in the vicinity of a single planar optical interface, as these situations are easier both to model and to implement, but increased flexibility would be provided by a stack of several layers of different materials. Eventually, a vast range of sophisticated experiments becomes available when non-planar optical environments are introduced, such as near-field tips or optical nano-antennas.

**Supporting Information**. A : polarization measurement protocol and theoretical calculations. B : description of the modelled experimental conditions. C : ratio between $A$, $B$ and $C$ coefficients. D : dependence of figure of merit $f_1$ on the experimental configuration. E : optimized configurations for polarized Fourier imaging analysis. F : non-polarized Fourier imaging : meaning of figures of merit $S$ and $D$, dependence on factors $\eta_{x,y,z}$. G : optimized configurations for non-polarized Fourier imaging.

**Corresponding Author**

*laurent.coolen@insp.jussieu.fr.

**References**

[1] W. E. Moerner and L. Kador, Optical detection and spectroscopy of single molecules in a solid, Phys. Rev. Lett. 62, 2535 (1989),

[2] M. Orrit and J. Bernard, Single pentacene molecules detected by fluorescence excitation in a p-terphenyl crystal, Phys. Rev. Lett. 65, 2716 (1990),

[3] S. A. Empedocles, R. Neuhauser, and M. G. Bawendi, Three-Dimensional Orientation Measurements of Symmetric Single Chromophores Using Polarization Microscopy, Nature (London) 399, 126 (1999),

[4] Inhee Chung, Ken T. Shimizu and Moungi G. Bawendi, Room temperature measurements of the 3D orientation of single CdSe quantum dots using polarization microscopy, PNAS 100, 405 (2003),

[5] X. Brokmann, L. Coolen, M. Dahan and J.-P. Hermier, Measurement of the radiative and nonradiative decay rates of single CdSe nanocrystals through a controlled modification of their spontaneous emission, Phys. Rev. Lett. 93, 107403 (2004),

[6] Elsa Cassette, Benoît Mahler, Jean-Michel Guigner, Gilles Patriarche, Benoît Dubertret and Thomas Pons, Colloidal CdSe/CdS dot-in-plate nanocrystals with 2D-polarized emission, ACS Nano 6, 6741 (2012),

[7] Riccardo Scott, Jan Heckmann, Anatol V. Prudnikau, Artsiom Antanovich, Aleksandr Mikhailov, Nina Owschimikow, Mikhail Artemyev, Juan I. Climente, Ulrike Woggon, Nicolai B. Grosse et al., Directed emission of CdSe nanoplatelets originating from strongly anisotropic 2D electronic structure, Nature Nanotech. 12, 1155 (2017),

[8] Yunan Gao, Mark C. Weidman and William A. Tisdale, CdSe nanoplatelet films with controlled orientation of their transition dipole moment, Nano Lett. 17, 3837 (2017),

[9] Fu Feng, Loan Thu Nguyen, Michel Nasilowski, Brice Nadal, Benoît Dubertret, Laurent Coolen and Agnès Maître, Consequence of shape elongation on emission asymmetry for colloidal CdSe/CdS nanoplatelets, Nano Research 11, 3593 (2018),

[10] R. J. Epstein, F. M. Mendoza, Y. K. Kato and D. D. Awschalom, Anisotropic interactions of a single spin and dark-spin spectroscopy in diamond, Nature Phys. 1, 94 (2005),

[11] Jiawen Liu, Lilian Guillemeney, Arnaud Choux, Agnès Maître, Benjamin Abécassis et Laurent Coolen, Fourier imaging of single self-assembled CdSe nanoplatelet chains and clusters reveals out-of-plane dipole contribution, ACS Photonics 7, 2825 (2020),

[12] Jon A. Schuller, Sinan Karaveli, Theanne Schiros, Keliang He, Shyuan Yang, Ioannis Kymissis, Jie Shan and Rashid Zia, Orientation of luminescent excitons in layered nanomaterials, Nature Nanotech. 8, 271 (2013),

[13] Mauro Brotons-Gisbert, Raphaël Proux, Raphaël Picard, Daniel Andres-Penares, Artur Branny, Alejandro Molina-Sanchez, Juan F. Sanchez-Royo and Brian D. Gerardot, Out-of-plane orientation of luminescent excitons in two-dimensional indium selenide, Nature Comm. 10:3913 (2019),

[14] Tim H. Taminiau, Sinan Karaveli, Niek F. van Hulst and Rashid Zia, Quantifying the magnetic nature of light emission, Nature Comm. 3, 979 (2012),

[15] Lukas Novotny and Bert Hecht, Principles of Nano-optics, Cambridge University Press (2006),

[16] Jiawen Liu, Lilian Guillemeney, Benjamin Abécassis and Laurent Coolen, Long range energy transfer in self-assembled stacks of semiconducting nanoplatelets, Nano Lett. 20, 3465 (2020),

[17] Whi Dong Kim, Dahin Kim, Da-Eun Yoon, Hyeonjun Lee, Jaehoon Lim, Wan Ki Bae and Doh C. Lee, Pushing the efficiency envelope for semiconductor nanocrystal-based electroluminescence devices using anisotropic nanocrystals, Chem. Mater. 31, 3066 (2019),

[18] Werner Trabesinger, Alois Renn, Bert Hecht, Urs P. Wild, Andrea Montali, Paul Smith and Christoph Weder, Single-molecule imaging revealing the deformation-induced formation of a polecular polymer blend, J. Phys. Chem. B 104, 5221 (2000),

[19] Xavier Brokmann, Marie-Virginie Ehrensperger, Jean-Pierre Hermier, Antoine Triller and Maxime Dahan, Orientational imaging and tracking of single CdSe nanocrystals by defocused microscopy, Chem. Phys. Lett. 406, 210 (2005),

[20] M. Ohmachi, Y. Komori, A. H. Iwane, F. Fujii, T. Jin, and T. Yanagida, Fluorescence Microscopy for Simultaneous Observation of 3D Orientation and Movement and its Application to Quantum Rod-Tagged Myosin V, Proc. Natl. Acad. Sci. U.S.A. 109, 5294 (2012),

[21] J. T. Fourkas, Rapid Determination of the Three-Dimensional Orientation of Single Molecules, Opt. Lett. 26, 211 (2001),

[22] Clotilde Lethiec, Julien Laverdant, Henri Vallon, Clémentine Javaux, Benoît Dubertret, Jean-Marc Frigerio, Catherine Schwob, Laurent Coolen and Agnès Maître, Measurement of three-dimensional dipole orientation of a single fluorescent nanoemitter by emission polarization analysis, Phys. Rev. X 4, 021037 (2014),

[23] M. Andreas Lieb, James M. Zavislan and L. Novotny, Single-molecule orientations determined by direct emission pattern imaging, J. Opt. Soc. Am. B 21, 1210 (2004),

[24] Fu Feng, Loan Thu Nguyen, Michel Nasilowski, Brice Nadal, Benoît Dubertret, Agnès Maître and Laurent Coolen, Probing the fluorescence dipoles of single cubic CdSe/CdS nanoplatelets with vertical or horizontal orientations, ACS Photonics 5, 1994 (2018),

[25] Jan Jasny and Jerzy Sepiol, Single molecules observed by immersion mirror objective. A novel method of finding the orientation of a radiating dipole. Chem. Phys. Lett. 273, 439 (1997),

[26] Andrew P. Bartko and Robert M. Dickson, Imaging three-dimensional single molecule orientations, J. Phys. Chem. B 103, 11237 (1999),

[27] Martin Böhmer and Jörg Enderlein, Orientation imaging of single molecules by wide-field epifluorescence microscopy, J. Opt. Soc. Am. B 20, 554 (2003),

[28] M. Lieberherr, Ch. Fattinger and W. Lukosz, Optical-environment-dependent effects on the fluorescence of submonomolecular dye layers on interfaces, Surf. Sci. 189, 954 (1987),

[29] J. Hohlbein and C. G. Hübner, Three-Dimensional Orientation Determination of the Emission Dipoles of Single Molecules: The Shot-Noise Limit, J. Chem. Phys. 129, 094703 (2008),

[30] Nhung C. Vu, Zakarya Ouzit, Clotilde Lethiec, Agnès Maître, Laurent Coolen, Frédéric Lerouge and Julien Laverdant, Single gold bipyramid orientation measured by plasmon-resonant scattering polarimetry, J. Phys. Chem. Lett. (2021),

[31] Robert M. Dickson, D. J. Norris and W. E. Moerner, Simultaneous imaging of individual molecules aligned both parallel and perpendicular to the optic axis, Phys. Rev. Lett. 81, 5322 (1998),

[32] J. J. Macklin, J. K. Trautman, T. D. Harris, and L. E. Brus, Imaging and Time-Resolved Spectroscopy of Single Molecules at an Interface, Science 272, 255 (1996),

[33] Jeongmo Kim, Reinaldo Chacon, Zijun Wang, Eric Larquet, Khalid Lahlil, Aymeric Leray, Gérard Colas-des-Francs, Jongwook Kim and Thierry Gacoin, Measuring 3D orientation of nanocrystals via polarized luminescence of rare-earth dopants, Nature Commun. 12, 1943 (2021),

[34] Jonathan A. Kurvits, Mingming Jiang and Rashid Zia, Comparative analysis of imaging configurations and objectives for Fourier microscopy, J. Opt. Soc. Am. A 11, 2082 (2015).

TOC graphic